OPEN ACCESS
Journal of Innovative Optical Health Sciences
(2025) 2540002 (12 pages)

DOI: 10.1142/S1793545825400024

World Scientific
www.worldscientific.com

Computer-guided optical clearing for transcranial laser speckle imaging of cortical blood flow through synergistic tartrazine-induced cranial bone transparency

Y. Surkov [*,†,‡‡], P. Timoshina [*,†,§§], I. Uvakin*, N. Shushunova [†], A. Konovalov [‡,§], I. Kozlov [‡], G. Piavchenko [¶], D. Telyshev [‡,‖], I. Meglinski [¶,**], S. Kuznetsov [¶] and V. Tuchin [*,†,††]

*Institute of Physics
Saratov State University, Saratov 410012, Russia

†Scientific Medical Center
Saratov State University, Saratov 410012, Russia

‡Institute for Bionic Technologies and Engineering
I.M. Sechenov First Moscow State Medical University,
Moscow 119991, Russia

§Burdenko Neurosurgery Institute, Moscow 125047, Russia

¶Department of Human Anatomy and Histology,
Cytology and Embryology Institute of Clinical Medicine N.V. Sklifosovsky
I.M. Sechenov First Moscow State Medical University,
Moscow 119991, Russia

‖Institute of Biomedical Systems
National Research University of Electronic Technology
Zelenograd, Moscow 124498, Russia

**Department of Mechanical, Biomedical & Design Engineering
College of Engineering & Physical Sciences, Aston University
Birmingham B4 7ET, UK

††Laboratory of Laser Molecular Imaging and Machine Learning
Tomsk State University, Tomsk 634050, Russia
‡‡surkov9898@gmail.com
§§timoshina2906@mail.ru

Received 7 August 2025
Accepted 10 October 2025
Published 5 November 2025

‡‡Corresponding author.

The clinical deployment of transcranial laser speckle-contrast imaging (LSCI) is limited by pronounced multiple scattering in cranial bone, which substantially reduces probing depth and distorts estimates of cerebral blood flow parameters. In this study, a hybrid strategy combining computational optical clearing (COC) with tartrazine-induced optical clearing of cranial bone is proposed and experimentally validated. Topical application of a 30% (w/v) tartrazine solution reduces the scattering coefficient of cranial bone from ~ 1.5 to $\sim 0.6\,\mathrm{mm}^{-1}$ by refractive index matching and by decreasing the intratissue heterogeneity of their spatial distribution. Residual quasi-static scattering components persisting after tartrazine-induced optical clearing are selectively removed by COC based on principal component analysis filtering, yielding an approximately twofold increase in vessel contrast-to-noise ratio (from 1.5 to 3.1) and exposing vascular networks invisible with conventional transcranial LSCI. This algorithm automatically ranks components in descending order of their contribution to the total variance: components with large eigenvalues correspond to quasi-static structures (cranial bone and stationary brain tissue), whereas those with small eigenvalues contain the dynamic signal arising from blood flow. Applying the Guttman–Kaiser criterion enables selective reconstruction of the dynamic component while suppressing background scattering. This synergistic approach opens new possibilities for noninvasive, high-contrast visualization of cerebral blood flow and represents a promising, qualitatively new direction in the development of physico-digital optical clearing technologies.

Keywords: Transcranial laser speckle-contrast imaging; optical clearing; principal component analysis; computational optical clearing; cerebral blood flow.

1. Introduction

Noninvasive imaging of cerebral blood flow plays a pivotal role in elucidating brain physiology, diagnosing neurological disorders such as stroke and neurodegenerative diseases, and monitoring therapeutic interventions in preclinical models.[1–3] Yet deep transcranial visualization of the cerebral cortex is severely hindered by pronounced multiple scattering of the probing light in cranial bone.[1,4] Laser speckle-contrast imaging (LSCI) is regarded as a promising noninvasive technique for mapping cerebral blood flow with high spatiotemporal resolution[1,5,6]; it analyzes speckle patterns generated when coherent light is scattered by moving erythrocytes.[7,8] However, under transcranial conditions, the probing depth is restricted to only a few hundred micrometers because of strong multiple scattering in cranial bone, which markedly reduces vascular contrast and often forces investigators to resort to invasive procedures such as craniotomy or skull thinning.[9] These interventions are highly invasive and undesirable, because cranial bone functions as a reservoir of immune cells that regulate meningeal immunity via specialized vascular channels.[9,10]

Over the past decade, optical approaches that reduce light scattering in biological tissues by refractive-index matching — collectively termed optical clearing (OC) methods — have been vigorously pursued.[11–14] Hyperosmolar agents, alcohol-sugar mixtures, and organic solvents decrease the extinction coefficient and thereby increase probing depth, as quantified by optical coherence tomography (OCT) and reconstructions of the scattering coefficient.[15,16] Recent studies have highlighted the potential of absorbing molecules as efficient optical clearing agents (OCAs).[17] For example, tartrazine — a biocompatible, FDA-approved food dye — has demonstrated high efficacy in achieving reversible tissue transparency by suppressing scattering in the visible and near-infrared spectral ranges without compromising safety.[17–20]

In parallel, computational approaches to enhance the contrast and penetration depth of LSCI have been actively developed. One promising strategy is a principal component analysis (PCA) based filter.[21,22] In this approach, a temporal sequence of speckle images is decomposed into an orthogonal basis, and each pixel is represented as a point in a multidimensional space whose coordinates correspond to its intensity in each frame. PCA automatically orders the principal components (PCs) by decreasing explained variance: components with large eigenvalues capture quasi-static structures

(cranial bone and stationary brain tissue), whereas those with small eigenvalues contain the dynamic speckle signal from moving erythrocytes.[21–24] Applying the Guttman–Kaiser criterion allows the static and dynamic constituents to be reconstructed separately, enabling selective suppression of scattering from immobile structures while retaining the vascular signal that remains inaccessible in standard full speckle-contrast analysis. Hereafter, the term computational optical clearing (COC) refers to this PCA-based filtering that selectively removes static scattering, in analogy to physical OC implemented algorithmically.

Despite considerable progress in OC and computational scattering-suppression methods, their potential has largely been explored in isolation. Combining OC, which physically reduces scattering in cranial bone, with COC based on PCA filtering, which mathematically eliminates residual scattering from stationary structures that remains after OC, is expected to yield a pronounced synergistic effect by extending probing depth and markedly enhancing contrast in minimally invasive transcranial LSCI.

This study, therefore, aims to evaluate the individual contributions of a 30% tartrazine solution and PCA filtering to improving the probing depth and quality of laser speckle-contrast images of cerebral vasculature through the intact mouse skull, and to validate, by OCT, the temporal dynamics of the accompanying reduction in the cranial bone scattering coefficient.

2. Materials and Methods

Experiments were performed on three adult male BALB/c mice (10–12 weeks; 25 ± 2 g). The study protocol was approved by the Ethics Committee of Saratov State Medical University named after V. I. Razumovsky, Ministry of Health of the Russian Federation (Protocol No. 11, 7 August 2022). All procedures complied with the ARRIVE 2.0 guidelines.[25] Mice were housed under a 12 h light/dark cycle (22 ± 1°C, 50 ± 5% humidity) with *ad libitum* access to food and water. Anesthesia was induced intraperitoneally with tiletamine + zolazepam (Zoletil® 100, Virbac, France; 10 mg/kg) and xylazine hydrochloride (Interchemie, Netherlands; 5 mg/kg). Depth of anesthesia was confirmed by the absence of pedal and corneal reflexes. Animals were secured in a custom 3D-printed stereotaxic holder. The scalp was surgically excised without damaging the periosteum, after which 200 μL of physiological saline was applied to the exposed skull to prevent dehydration.

One mouse was allocated to transcranial LSCI monitoring, and the remaining two were used for OCT monitoring at central wavelengths of 930 nm and 1325 nm, respectively.

An aqueous 30% (w/v) solution of tartrazine (E102, Sigma Aldrich, ≥ 97% purity) containing 0.625% (w/v) hydroxyethyl cellulose (Shin-Etsu, Germany) was used as the OCA; the polymer acted as a gelling agent to reduce water evaporation. The mixture was heated to 70°C and stirred with a magnetic stirrer for 10 min until complete homogenization had been achieved, after which it was allowed to cool in the tube to room temperature (25 ± 2°C). Next, 150 μL of the OCA was applied evenly to the exposed skull with a pipette and covered with a coverslip to prevent evaporation and tartrazine precipitation.[17,18]

The choice of a 30% (w/v) aqueous tartrazine solution was motivated by the absorbing-dye mechanism of tissue transparency, which increases the real part of the refractive index in the red spectral band via Kramers–Kronig relations and thereby reduces scattering most strongly at $\lambda \approx 600$–650 nm (i.e., the LSCI band).[17] Unlike hyperosmotic OCAs (e.g., glycerol), which, in addition to bulk RI-matching, rely on a dehydration mechanism and typically require high concentrations for effective OC, resulting in high OCA viscosity and hence slower diffusion, the absorbing-dye approach yields a rapid effect at moderate concentrations. Considering the experimentally reported exponential decrease of solution stability with increasing tartrazine concentration, we used 0.625% hydroxyethyl cellulose and a coverslip to suppress evaporation and precipitation, ensuring ≥ 25 min of stable action *in vivo*.[17,18]

The LSCI system consisted of a 632 nm He-Ne laser (20 mW, 15 mm beam diameter), a zoom objective lens, and a Thorlabs sCMOS camera (1920×1200 px, 8 bit). The effective field of view was 1.6×1.0 cm, yielding a pixel size of ≈ 8 μm. Sequences of 200 frames were recorded at 30 fps with an exposure time of 5 ms.

Spatiotemporal full speckle contrast (K_{full}) was computed from the raw speckle images (RSIs) using a 7×7 pixel spatial window and a 100-frame temporal window (Eq. (1)).[8,21]

$$K_{\text{full}} = \sigma_{S,T}/\langle I\rangle_{S,T}. \quad (1)$$

Here $\langle I\rangle_{S,T}$ and $\sigma_{S,T}$, denote the mean intensity and its standard deviation, respectively, evaluated over the spatial window S (7×7 pixels) and temporal window T (100 consecutive frames).

To separate the static and dynamic components of the speckle signal, a PCA-based filtering algorithm was applied.[21] Each raw speckle image (RSI) was vectorized into a column vector, producing an $M \times N$ data matrix ($M = 2,304,000$ pixels; $N =$ 100 consecutive RSIs). PCs were extracted and classified as static or dynamic according to the Guttman–Kaiser criterion: components whose eigenvalues exceeded the mean were assigned to the static set. The quasi-static speckle signal was reconstructed from these static components, and the dynamic signal was obtained by subtracting the static reconstruction from the original data. In our 100-frame recordings, the quasi-static set typically comprised $\sim$ 5–20 PCs, and the rest formed the dynamic set.

Static speckle-contrast maps (K_{static}) were calculated from the reconstructed static RSI stack, whereas the dynamic speckle contrast (K_{dynamic}) was defined as the difference K_{full} and K_{static}. Relative blood flow index (rBFI) maps were obtained by inverting the squared speckle contrast in the short-exposure regime:

$$\text{rBFI}_{\text{full}} = 1/K^2_{\text{full}}, \quad \text{rBFI}_{\text{dynamic}} = 1/K^2_{\text{dynamic}}. \quad (2)$$

This definition exploits the inverse-square proportionality between speckle contrast and scatterer velocity when the camera exposure time is shorter than the decorrelation time of erythrocyte motion.[8,21]

The visibility of individual vessels was quantified by calculating the contrast-to-noise ratio (CNR) for both the full speckle-contrast maps and the PCA-filtered dynamic component. CNR at a given time t was defined as

$$\text{CNR}(t) = (\langle K_{\text{ROI}}(t)\rangle - \langle K_{\text{bg}}(t)\rangle)/\sigma_{\text{bg}}, \quad (3)$$

where $\langle\cdot\rangle$ denotes the mean value within the vessel region of interest (ROI), bg denotes a neighboring parenchymal background area free of large vessels, and σ_{bg} is the standard deviation within that background. ROI masks were delineated manually in ImageJ on the speckle-contrast maps. Five cortical vessels of comparable diameter ($120 \pm 50\,\mu$m) were then selected; their centerlines were separated by at least $400\,\mu$m to ensure independent noise sampling. For each vessel the background region was defined by a concentric annulus whose width exceeded $200\,\mu$m.

A commercial swept-source optical coherence tomography (SS-OCT) system, OCS1300SS (Thorlabs, USA; central wavelength 1325 nm, spectral bandwidth 100 nm), was used together with a spectral-domain OCT system, GAN930V2 BU (Thorlabs, USA; axial resolution $5.34\,\mu$m in air, central wavelength 930 nm). Each mouse underwent seven imaging sessions: before application of the OCA (0 min) and at 1, 5, 10, 15, 20, and 25 min thereafter.

To quantify tartrazine-induced changes in the optical properties of the skull, depth-resolved maps of the scattering coefficient (μ_s) were reconstructed from the OCT data. Custom Python software implementing the algorithm described in Ref. 26 was developed for this purpose. The reconstruction is based on a single-scattering model and corrects for the axial point spread function (APSF) of the OCT system.

To accurately assess the optical characteristics of the samples using OCT, it was crucial to account for the influence of the APSF ($h(z)$), which is determined by the optics of the OCT system. The recorded depth profile of the OCT signal ($I(z)$) can be described using the following equation[25]:

$$I(z) = h(z) \cdot \exp(-2\mu_s z), \quad (4)$$

where $\mu_s(z)$ is the scattering coefficient as a function of depth z.

The APSF in the context of OCT is described by the following function[25]:

$$h(d) = \frac{1}{\left(\frac{d}{z_i}\right)^2 + 1}, \quad z_i = \frac{\pi n \omega_i^2}{\lambda_0}, \quad (5)$$

where $d = z - z_f$ is the distance of the reflecting object from the focal plane position z_f, z_i is the Rayleigh length in the ith layer of the sample, n is the group refractive index of the sample, ω_i is the waist radius at the focus (lateral OCT resolution), and λ_0 is the central wavelength of the OCT probing radiation.

To reconstruct the depth-resolved scattering coefficient $\mu_s(z)$ of the probing light, considering the discreteness of the signal, the following equation was used[25]:

$$\mu_s(i) = \frac{I(i)}{2\delta \sum_{i+1}^{N} I(i)}, \quad (6)$$

where Δ is the pixel size in the axial direction; $I(i)$ is the intensity of the OCT signal at the ith pixel; and N is the total number of pixels in the axial direction.

From the μ_s maps, an ROI was selected to extract an average depth profile of μ_s, enabling the temporal evolution of the OCA effect to be monitored at different cranial depths.

3. Results

Speckle-contrast maps of the full (K_{full}), static (K_{static}), and dynamic (K_{dynamic}) components obtained before and during OC are shown in Fig. 1. They reveal a progressive reduction in static scattering and a more homogeneous distribution of the dynamic component. Within 1 min of OCA application, the high contrast regions associated with superficial scattering structures (green arrows in the K_{full}) had almost disappeared, indicating the early onset of partial clearing of the outer skull layers. Continued exposure to the OCA (5–25 min) produced a gradual decrease in both the intensity and the area of regions with elevated K_{full} corresponding to cranial bone (red arrows), suggesting deep clearing of the compact bone layers. Concurrently, K_{static} values declined in proportion to the reduction in scattering, whereas the K_{dynamic} map preserved the vascular pattern and strongly suppressed scattering from stationary tissues. Thus, superficial scattering was markedly reduced within the first 5 min, and by 25 min, skull-related scattering was substantially suppressed, enabling long-term monitoring of cerebral hemodynamics with enhanced optical contrast.

Full speckle-contrast maps (K_{full}) and the corresponding dynamic-component maps (K_{dynamic}) acquired before, and at 1 min and 25 min after, OCA application are shown in Fig. 2. After 25 min of OC, previously hidden vascular structures became visible within ROI 2 (green frame; red arrows). In the associated K_{dynamic} map, superficial scattering was further suppressed, which enhanced vessel visibility. PCA filtering provided an additional benefit: static artifacts produced by air bubbles in the OCA or residual hairs on the skull surface (yellow arrows in ROI 1) were completely eliminated in K_{dynamic} while the vascular pattern was retained. Several vessels that were undetectable in K_{full} became discernible after COC (blue arrows), and physical OC amplified this effect. The combined application of OC and COC unveiled an extended vascular network (green arrows) that was indistinguishable either before OCA treatment or with PCA filtering alone.

Consequently, the combined application of OC and COC produces a pronounced synergistic effect: scattering from static cranial structures is suppressed much more efficiently than with either technique alone, as evidenced by the near-complete disappearance of high contrast K_{full} regions and the enhanced visibility of cerebral vessels.

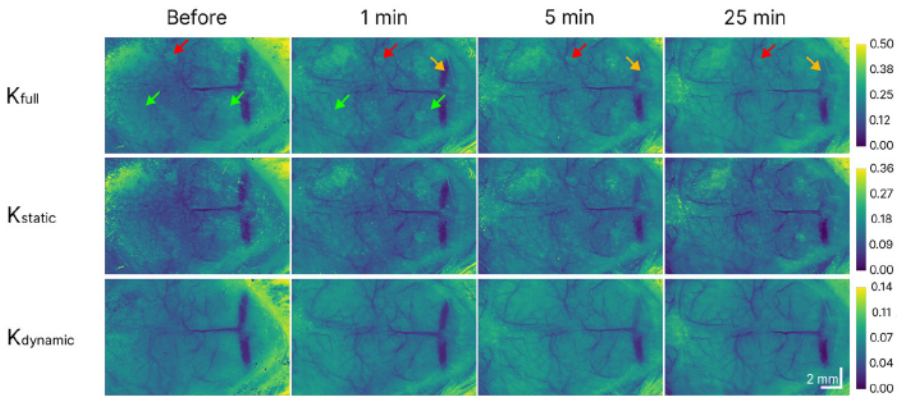

Fig. 1. Speckle-contrast maps obtained before and at 1, 5, and 25 min after the onset of OC. The top, middle, and bottom rows show the full speckle contrast (K_{full}), static component (K_{static}), and dynamic component (K_{dynamic}), respectively. Red arrows denote regions of high K_{full} arising from scattering in cranial bone; both their intensity and area decrease progressively during clearing. Green arrows highlight superficial high contrast scattering zones that disappear within the first minute. Orange arrows mark a small area near the coverslip edge where the tartrazine solution inadvertently contacted air, leading to local precipitation and a strongly scattering artifactual zone; this artifact transiently increased K_{static} (and thus K_{full}) and was excluded from quantitative analysis. Separate colorbars are shown on the right for each contrast type (arbitrary units).

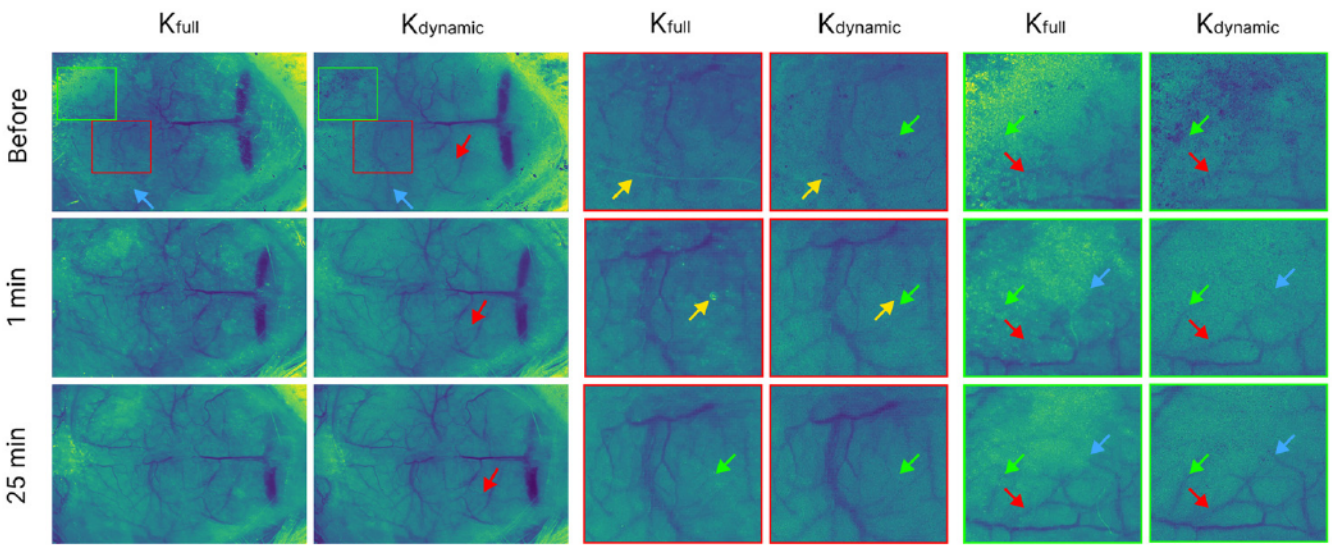

Fig. 2. Comparison of full (K_{full}) and dynamic ($K_{dynamic}$) speckle-contrast maps acquired before, and 1 min and 25 min after, application of the OCA. The original maps with the regions of interest — ROI 1 (red outline) and ROI 2 (green outline) — are shown on the left; enlarged views of these regions are shown on the right. Yellow arrows indicate artifacts removed by COC; green arrows mark vessels discernible only after the combined application of physical OC and PCA filtering; red arrows denote vessels revealed by OC alone; blue arrows point to vessels uncovered by COC alone.

Figure 3 illustrates how OC and COC influence the symmetry of speckle-contrast values in mirror-symmetric cortical regions of the mouse. Prior to application of the OCA, K_{full} values in the two symmetric ROIs differ markedly, indicating uneven superficial scattering by the skull. Within 1 min of OC this disparity diminishes, and by 25 min it is essentially eliminated, reflecting a progressive equalization of the cranial optical properties. A different behavior is observed for the dynamic component ($K_{dynamic}$). Although its values initially diverge between ROIs, the combined application of OC and COC removes these discrepancies almost immediately, rendering the contrast in both regions comparable at the earliest stage of OC. Accordingly, the two techniques together effectively negate the influence of static scattering and provide a more accurate, spatially uniform assessment of cerebral perfusion.

Figure 4 compares K_{static}, relative blood flow indices derived from the full ($rBFI_{full}$) and dynamic ($rBFI_{dynamic}$) speckle-contrast data, and their difference (ΔrBFI) acquired before OC and at 1 min and 25 min thereafter. Dashed outlines delineate regions dominated by static skull scattering. Prior to OC, $rBFI_{full}$ underestimates flow in areas of high K_{static} relative to adjacent and mirror symmetric brain regions, whereas $rBFI_{dynamic}$ faithfully reflects the vascular pattern and yields flow values comparable to those elsewhere in the mouse brain. This confirms that COC effectively suppresses the contribution of statically scattering bone and enables a more accurate assessment of perfusion in transcranial LSCI. Moreover, the area and prominence of highly scattering zones decrease markedly within 1 min after application of the 30% tartrazine solution and have virtually disappeared by 25 min. In the ΔrBFI maps, this appears as a pronounced attenuation of brightness within the contours, indicating equalization of bone optical density and reduced variability of static scattering.

Figure 5 shows composite pseudocolor maps of the rBFI: values obtained from the dynamic component after PCA filtering are encoded in the red channel, whereas rBFI calculated from the full speckle-contrast is encoded in the green channel. Before OC (left panel), extensive red regions are present, indicating that rBFI derived from the full contrast underestimates blood-flow velocity in areas where static skull scattering dominates. Within 1 min of OCA application, most vessels appear yellow, reflecting the convergence of the two estimates. By 25 min (right panel), the vascular network is almost entirely yellow, signifying that static-scattering artifacts have been minimized and that perfusion estimates from both approaches are in close agreement. Thus, OC substantially reduces regions in which blood flow is underestimated, while

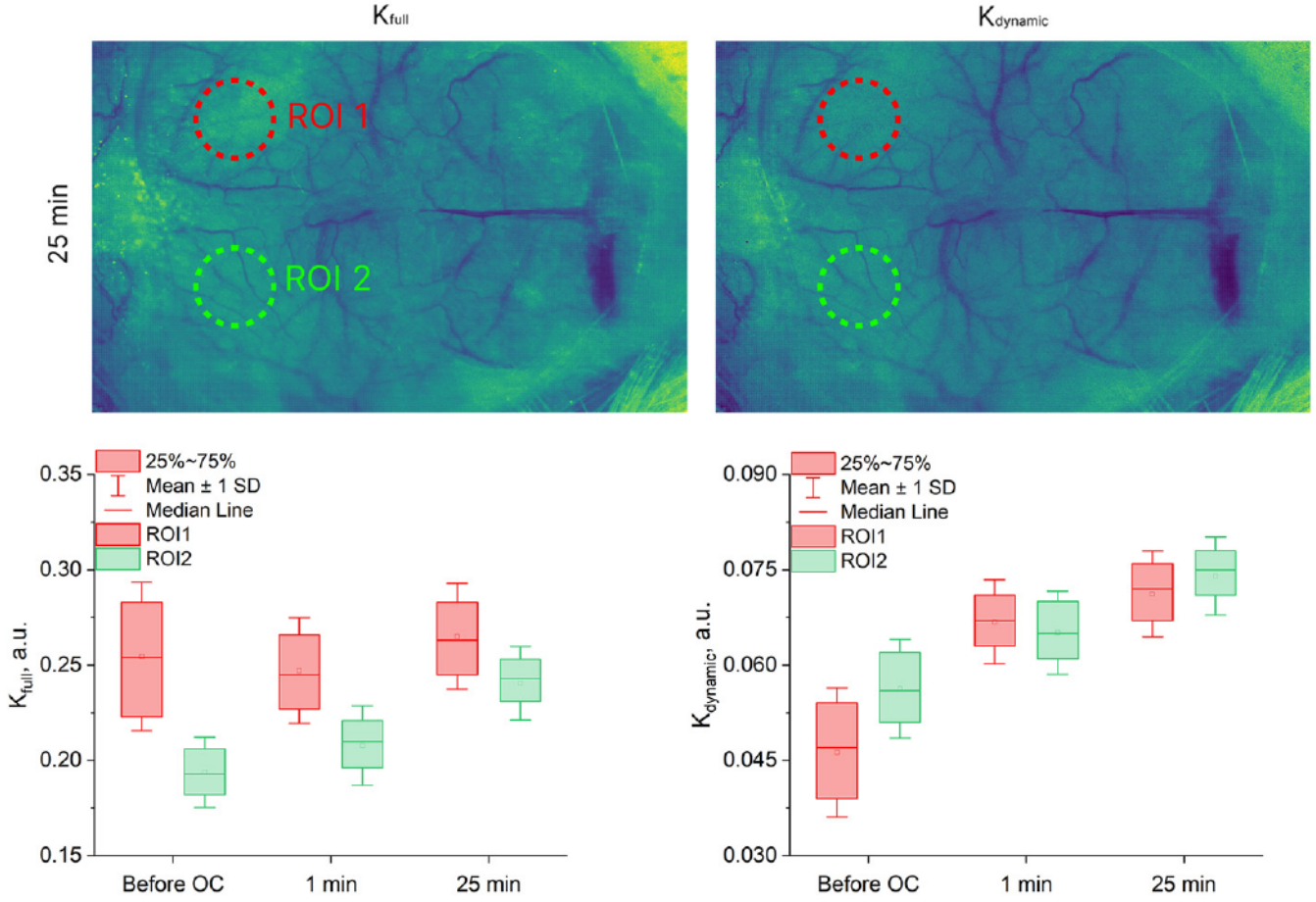

Fig. 3. K_{full} and $K_{dynamic}$ maps with mirror-symmetric regions of interest — ROI 1 (red dashed circle) and ROI 2 (green dashed circle) — together with the corresponding value distributions obtained before OC and at 1 min and 25 min thereafter.

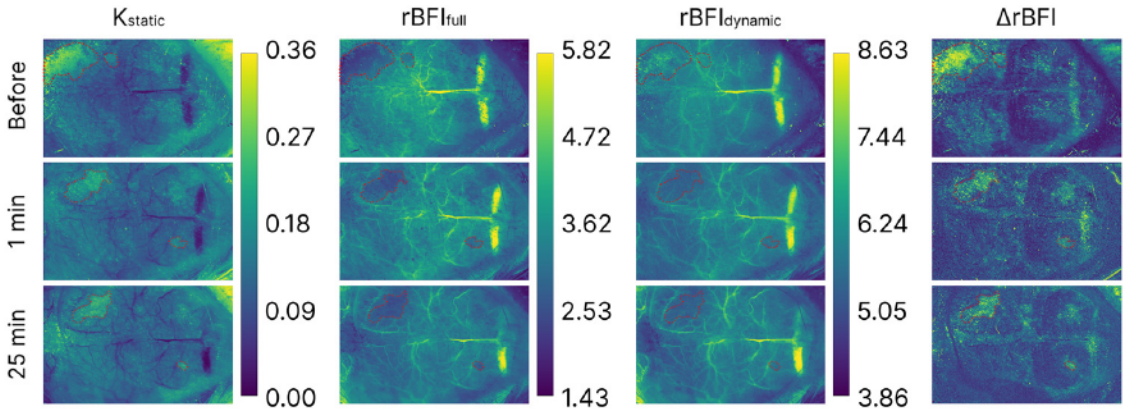

Fig. 4. K_{full}; relative blood flow indices derived from the full ($rBFI_{full}$) and dynamic ($rBFI_{dynamic}$) speckle-contrast data; and their difference (ΔrBFI) acquired before OC and at 1 min thereafter. The rBFI maps are shown on a logarithmic scale. Dashed contours delineate regions that exhibited high K_{static} prior to clearing, reflecting strong static scattering by the skull. After clearing these contours shrink — most conspicuously in the ΔrBFI maps. PCA filtering yields more homogeneous $rBFI_{dynamic}$ maps by suppressing bone scattering artifacts and thereby improving the accuracy of transcranial perfusion assessment.

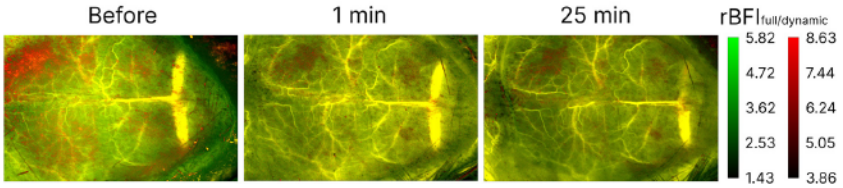

Fig. 5. Pseudocolor maps of the rBFI acquired before OC and at 1 min and 25 min thereafter. The red channel encodes $rBFI_{dynamic}$, whereas the green channel represents $rBFI_{full}$. Red regions mark areas where $rBFI_{full}$ underestimates blood-flow velocity relative to $rBFI_{dynamic}$; their size and intensity diminish markedly within 1 min of OC and have virtually disappeared by 25 min, demonstrating effective suppression of static skull scattering by OC.

the PCA-filtered dynamic analysis remains the most robust to bone-related artifacts.

Taken together, the results confirm a synergistic effect between OC and COC: OC mitigates the artifact source itself (scattering), and PCA filtering removes its residual contributions, yielding a reliable, spatially homogeneous map of cerebral blood flow.

Figure 6(a) illustrates the temporal evolution of CNR_{full} and $CNR_{dynamic}$ averaged across five cortical vessels of comparable diameter ($120 \pm 50\,\mu m$). Within 1 min after application of the 30% tartrazine solution, CNR_{full} increased from 1.5 ± 0.3 to 2.7 ± 0.4, whereas $CNR_{dynamic}$ reached 2.8 ± 0.4. Both metrics plateaued at ≈ 3.0 after ~ 20 min and remained stable for the remainder of the 25-min observation period. Shaded areas represent $\pm$ standard deviation ($n = 5$ vessels). Figure 6(b) summarizes the cumulative gain in CNR. OC alone enhanced CNR by 94% at 25 min, while the combined OC + COC protocol produced a 104% increase. PCA filtering alone prior to OCA application raised CNR by 31% on average. The quantitative analysis confirms the high efficacy of the hybrid strategy: COC provides an immediate contrast boost, while OC consolidates the effect, yielding a twofold CNR increase over baseline.

OCT monitoring revealed how OC alters the optical properties of the mouse skull (Figs. 7 and 8). Prior to OCA application, the initial B-scan (Fig. 7) displayed two pronounced layers: a superficial layer with strong back-scattering attributable to high mineralization and a deeper layer with markedly weaker scattering. 5 min after agent application, the scattering amplitude in the first layer had decreased, and by 20–25 min it was comparable to that of the second layer ($\mu_s \approx 0.6$–$0.8\,mm^{-1}$). Concurrently, the pronounced brightness gradient

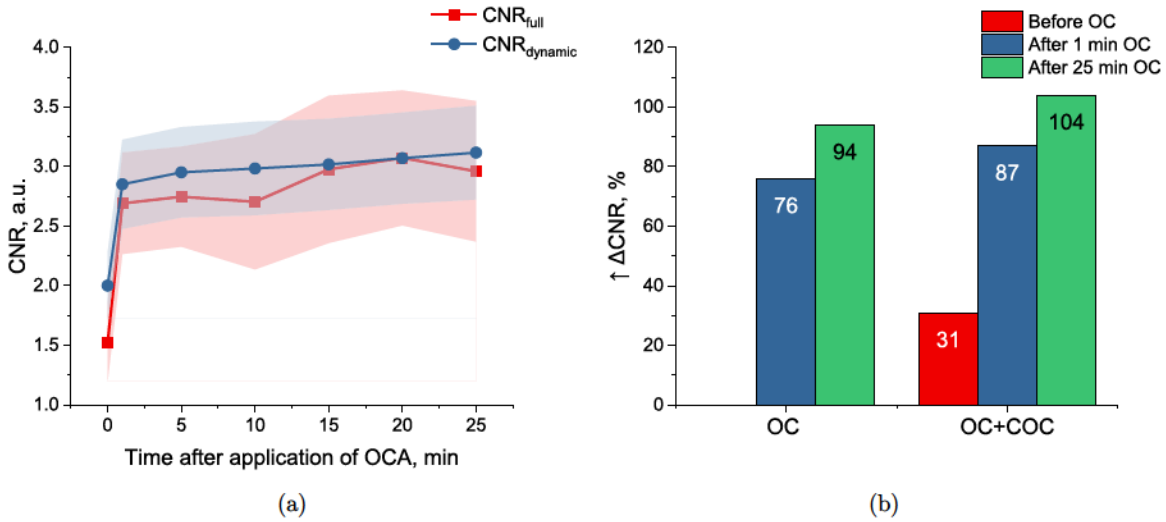

Fig. 6. Quantitative impact of OC and COC on vascular contrast. (a) Temporal evolution of the CNR calculated from K_{full} (CNR_{full}) and from $K_{dynamic}$ images after COC ($CNR_{dynamic}$). Curves show the mean $\pm$ SD for five cortical vessels of comparable diameter ($120 \pm 50\,\mu m$; $n = 5$). (b) Relative CNR gain (ΔCNR) obtained with OC alone and with the combined OC + COC protocol.

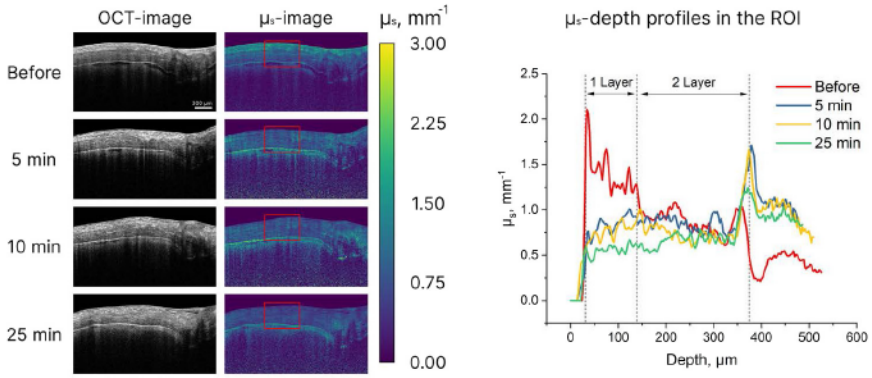

Fig. 7. Temporal evolution of OC in the mouse skull assessed by OCT-930 nm. Left: raw OCT B-scans (dynamic range of each image normalized for display) and their corresponding scattering-coefficient maps (μ_s); the red rectangle delineates the region from which depth profiles were extracted. Right: depth-resolved μ_s profiles recorded at various time points after OCA application.

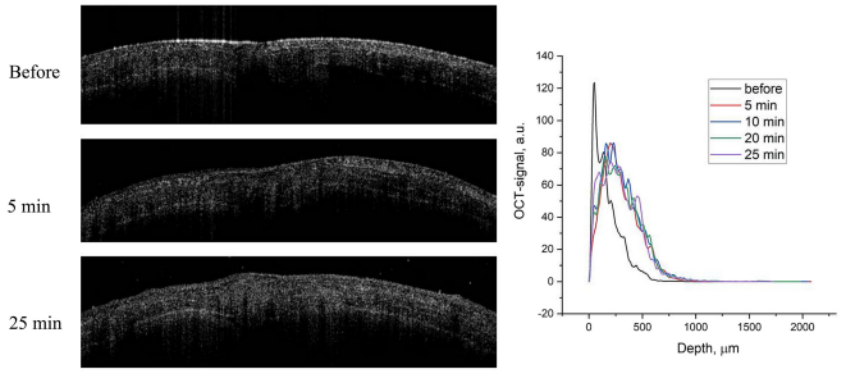

Fig. 8. Dynamics of OC of the mouse skull according to OCT-1325 nm data. Left: original OCT scans, visualization window size 3×8 mm. Right: depth profiles of the OCT signal at different time points after OCA application.

in structural OCT images vanished, indicating that the optical properties had become uniform across the skull thickness. Depth-resolved μ_s profiles extracted from the ROI confirmed the selective action of the OCA: the greatest reduction occurred in the first layer, whereas the scattering coefficient in the second layer changed only slightly. Thus, OC predominantly affects the superficial, highly mineralized portion of the bone, improving its optical homogeneity and thereby increasing skull transparency for visualizing cerebral structures.

4. Discussion

While this study targets the red band ($\lambda = 632$ nm) to leverage the strongest tartrazine-induced reduction of scattering, near-infrared (700–850 nm) illumination typically exhibits lower tissue scattering and can increase photon penetration. Porting the OC + COC protocol to NIR could thus extend probing depth, albeit with trade-offs: weaker dye-induced transparency in the NIR and reduced camera quantum efficiency. Cross-polarization gating would further mitigate surface glare at the expense of the detected photon budget. Future work will therefore evaluate NIR implementations and polarization gating, as well as absorbing-dye formulations with red-to-NIR-skewed spectra.

This proof-of-concept study combined tartrazine-enabled OC with PCA-based COC *in vivo*. LSCI quantification was performed across multiple vascular ROIs in one mouse, and OCT tracking of cranial μ_s dynamics involved two additional animals at 930 nm and 1325 nm. The small sample size limits statistical power and generalizability. Inter-animal variability — calvarial thickness and mineralization, age/strain, and anatomical site — likely modulates clearing kinetics and the degree of residual quasi-static scattering. Prior studies[27,28] report that mouse skull thickness increases with age

and that older skulls exhibit higher optical attenuation compared with juvenile skulls — factors that can hinder transcranial imaging and prolong the time required to reach an effective OC state. Accordingly, future work will increase the cohort size, phenotype skull properties (e.g., OCT-based thickness mapping) to assess robustness across conditions.

Our PCA-based COC relies on variance ordering and the GK criterion to isolate quasi-static variance (bone, stationary tissue, glare) from the dynamic speckle component. In 100-frame stacks, the quasi-static set usually comprised 5–20 PCs; adding more frames marginally improved stability but increased computation. Alternative filters[29,30] are promising but typically require longer sequences or task-specific priors; here, PCA offered a training-free, computationally efficient baseline that already maximized the synergy with OC.

5. Conclusion

In this study, we demonstrated a synergistic improvement of transcranial LSCI by combining OC with a 30% tartrazine solution and COC based on PCA filtering. Accordingly, the OC + COC protocol yielded an approximately twofold CNR increase (+104%) and exposed vessels invisible with conventional transcranial LSCI. OC reduced the cranial bone scattering coefficient from ~ 1.5 to $\sim 0.6\,\mathrm{mm}^{-1}$ and achieved optical homogeneity within 20–25 min, whereas COC selectively suppressed residual contributions from static structures, thereby minimizing artifacts and enhancing vessel visibility. When applied together, the two approaches markedly increased probing depth and image quality, equalized rBFI estimates, and exposed vascular networks that were invisible with conventional LSCI through the intact skull.

These results corroborate the synergy hypothesis: OC mitigates the primary scattering source, while COC removes its residual signal components, yielding a more accurate and spatially uniform assessment of cerebral perfusion. The findings are consistent with previous studies on tissue OC and digital LSCI processing and constitute the first demonstration of their joint use for minimally invasive visualization of cerebral blood flow in laboratory mice.

Acknowledgment

This work was financially supported by a grant from the Russian Science Foundation No. 22-65-00096.

Conflicts of Interest

The authors declare no conflicts of interest (financial or non-financial) related to this work.

Availability of data and materials

The data and materials that support the findings of this study are available from the corresponding author upon reasoning request.

ORCID

Y. Surkov https://orcid.org/0000-0001-6736-4480
P. Timoshina https://orcid.org/0000-0003-4856-9522
N. Shushunova https://orcid.org/0000-0001-5366-1783
A. Konovalov https://orcid.org/0000-0002-0932-4752
I. Kozlov https://orcid.org/0000-0002-4625-9267
G. Piavchenko https://orcid.org/0000-0001-7782-3468
D. Telyshev https://orcid.org/0000-0002-4221-9882
I. Meglinski https://orcid.org/0000-0002-7613-8191
S. Kuznetsov https://orcid.org/0000-0002-0704-1660
V. Tuchin https://orcid.org/0000-0001-7479-2694

References

1. E. Zherebtsov, A. Sdobnov, O. Sieryi, M. Kaakinen, L. Eklund, T. Myllylä, A. Bykov, I. Meglinski, "Enhancing transcranial blood flow visualization with dynamic light scattering technologies: Advances in quantitative analysis," *Laser Photonics Rev.* 19(2), 2401016 (2025).
2. A. Konovalov, V. Gadzhiagaev, F. Grebenev, D. Stavtsev, G. Piavchenko, A. Gerasimenko, D. Telyshev, I. Meglinski, S. Eliava, "Laser speckle

contrast imaging in neurosurgery: A systematic review," *World Neurosurg.* **171**, 35–40 (2023).
3. A. Konovalov, F. Grebenev, D. Stavtsev, I. Kozlov, V. Gadjiagaev, G. Piavchenko, D. Telyshev, A. Yu. Gerasimenko, I. Meglinski, S. Zalogin, A. Artemyev, G. Golodnev, T. Shumeiko, S. Eliava, "Real-time laser speckle contrast imaging for intraoperative neurovascular blood flow assessment: Animal experimental study," *Sci. Rep.* **14**, 1735 (2024).
4. J. Liu, H. Xu, S. Gao, L. Liu, J. Qu, T. Y. Ohulchanskyy, "Combining near infrared fluorescence and laser speckle imaging with optical tissue clearing for *in vivo* transcranial monitoring of cerebral blood vessels damaged by photodynamic nanoformulation," *Biomed. Opt. Express* **15**(2), 924–937 (2024).
5. G. Piavchenko, I. Kozlov, V. Dremin, D. Stavtsev, E. Seryogina, K. Kandurova, V. Shupletsov, K. Lapin, A. Alekseyev, S. Kuznetsov, A. Bykov, A. Dunaev, I. Meglinski, "Impairments of cerebral blood flow microcirculation in rats brought on by cardiac cessation and respiratory arrest," *J. Biophotonics* **14**(12), e202100216 (2021).
6. A. Sdobnov, V. Tsytsarev, G. Piavchenko, A. Bykov, I. Meglinski, "Beyond life: Exploring hemodynamic patterns in postmortem mice brains," *J. Biophotonics* **17**(7), e202400017 (2024).
7. I. Meglinski, A. Dunn, T. Durduran, D. Postnov, D. Zhu, "Dynamic light scattering in biomedical applications: Feature issue introduction," *Biomed. Opt. Express* **15**(5), 2890–2897 (2024).
8. A. Sdobnov, G. Piavchenko, A. Bykov, I. Meglinski, "Advances in dynamic light scattering imaging of blood flow," *Laser Photonics Rev.* **18**(2), 2300494 (2024).
9. W. Feng, C. Liu, L. Wang, C. Zhang, "An optical clearing imaging window: Realization of mouse brain imaging and manipulation through scalp and skull," *J. Cereb. Blood Flow Metab.* **43**(12), 2105–2119 (2023).
10. S. Brioschi, W.-L. Wang, V. Peng, M. Wang, I. Shchukina, Z. J. Greenberg, J. K. Bando, N. Jaeger, R. S. Czepielewski, A. Swain, D. A. Mogilenko, W. L. Beatty, P. Bayguinov, J. A. J. Fitzpatrick, L. G. Schuettpelz, C. C. Fronick, I. Smirnov, J. Kipnis, V. S. Shapiro, G. F. Wu, S. Gilfillan, M. Cella, M. N. Artyomov, S. H. Kleinstein, M. Colonna, "Heterogeneity of meningeal B cells reveals a lymphopoietic niche at the CNS borders," *Science* **373**(6553), eabf9277 (2021).
11. T. Yu, J. Zhu, D. Li, D. Zhu, "Physical and chemical mechanisms of tissue optical clearing," *iScience* **24**(3), 102178 (2021).
12. T. Yu, X. Zhong, D. Li, J. Zhu, V. V. Tuchin, D. Zhu, "Delivery and kinetics of immersion optical clearing agents in tissues: Optical imaging from *ex vivo* to *in vivo*," *Adv. Drug Deliv. Rev.* **215**, 115470 (2024).
13. J. Zhu, X. Liu, Y. Deng, D. Li, T. Yu, D. Zhu, "Tissue optical clearing for 3D visualization of vascular networks: A review," *Vasc. Pharmacol.* **141**, 106905 (2021).
14. D. Zhu, V. V. Tuchin, "Tissue optical clearing imaging from *ex vivo* toward *in vivo*," *BME Front.* **5**, 0058 (2024).
15. M. Varaka, M. Z. Vardaki, G. Gaitanis, I. D. Bassukas, N. Kourkoumelis, "The effect of different optical clearing agents on the attenuation coefficient and epidermal thickness of human skin assessed by optical coherence tomography," *Appl. Sci.* **12**(16), 8277 (2022).
16. P. A. Moldon, P. B. Ermolinskiy, A. E. Lugovtsov, P. A. Timoshina, E. N. Lazareva, Y. I. Surkov, Y. I. Gurfinkel, V. V. Tuchin, A. V. Priezzhev, "Influence of optical clearing agents on the scattering properties of human nail bed and blood microrheological properties: *In vivo* and *in vitro* study," *J. Biophotonics* **17**, e202300524 (2024).
17. Z. Ou, Y.-S. Duh, N. J. Rommelfanger, C. H. C. Keck, S. Jiang, K. Brinson, Jr., S. Zhao, E. L. Schmidt, X. Wu, F. Yang, B. Cai, H. Cui, W. Qi, S. Wu, A. Tantry, R. H. Roth, J. B. Ding, X. Chen, J. A. Kaltschmidt, M. L. Brongersma, G. Hong, "Achieving optical transparency in live animals with absorbing molecules," *Science* **385**(6713), eadm6869 (2024).
18. A. R. Guerra, L. R. Oliveira, G. O. Rodrigues, M. R. Pinheiro, M. I. Carvalho, V. V. Tuchin, L. M. Oliveira, "Tartrazine for optical clearing of tissues: Stability and diffusion issues," *J. Biophotonics* **18**, e202500160 (2025).
19. D. A. Miller, Y. Xu, R. Highland, V. T. Nguyen, W. J. Brown, G. Hong, J. Yao, A. Wax, "Enhanced penetration depth in optical coherence tomography and photoacoustic microscopy *in vivo* enabled by absorbing dye molecules," *Optica* **12**(1), 24–30 (2025).
20. A. Narawane, R. Trout, C. Viehland, A. N. Kuo, L. Vajzovic, A. H. Dhalla, C. A. Toth, "Optical clearing with tartrazine enables deep transscleral imaging with optical coherence tomography," *J. Biomed. Opt.* **29**(12), 120501 (2024).
21. Y. Surkov, P. Timoshina, I. Serebryakova, D. Stavtcev, I. Kozlov, G. Piavchenko, I. Meglinski, A. Konovalov, D. Telyshev, S. Kuznetcov, E. Genina, V. Tuchin, "Laser speckle contrast imaging with principal component and entropy analysis: A novel approach for depth-independent blood flow assessment," *Front. Optoelectron.* **18**(1), 1–19 (2025).

22. A. Arias-Cruz, R. Chiu, H. Peregrina-Barreto, R. Ramos-Garcia, T. Spezzia-Mazzocco, J. C. Ramirez-San-Juan, "Visualization of in vitro deep blood vessels using principal component analysis based laser speckle imaging," *Biomed. Opt. Express* **10**, 2020–2031 (2019).
23. M. Wang, C. Guan, W. Mao, H. Xiong, H. Tan, D. Hang, Y. Zeng, "Real-time full-field optical angiography utilizing principal component analysis," *Opt. Lett.* **43**(11), 2559–2562 (2018).
24. C. Li, R. Wang, "Dynamic laser speckle angiography achieved by eigen-decomposition filtering," *J. Biophoton.* **10**, 805–810 (2017).
25. N. Percie du Sert, V. Hurst, A. Ahluwalia, S. Alam, M. T. Avey, M. Baker, W. J. Browne, A. Clark, I. C. Cuthill, U. Dirnagl, M. Emerson, P. Garner, S. T. Holgate, D. W. Howells, N. A. Karp, S. E. Lazic, K. Lidster, C. J. MacCallum, M. Macleod, E. J. Pearl, O. H. Petersen, F. Rawle, P. Reynolds, K. Rooney, E. S. Sena, S. D. Silberberg, T. Steckler, H. Würbel, "The ARRIVE guidelines 2.0: Updated guidelines for reporting animal research," *J. Cereb. Blood Flow Metab.* **40**, 1769–1777 (2020).
26. J. Liu, N. Ding, Y. Yu, X. Yuan, S. Luo, J. Luan, Y. Zhao, Y. Wang, Z. Ma, "Optimized depth-resolved estimation to measure optical attenuation coefficients from optical coherence tomography and its application in cerebral damage determination," *J. Biomed. Opt.* **24**(3), 035002 (2019).
27. Y. J. Zhao, T. T. Yu, C. Zhang, Z. Li, Q. M. Luo, T. H. Xu, D. Zhu, "Skull optical clearing window for *in vivo* imaging of the mouse cortex at synaptic resolution," *Light Sci. Appl.* **7**, 17153 (2018).
28. H. Soleimanzad, H. Gurden, F. Pain, "Optical properties of mice skull bone in the 455- to 705-nm range," *J. Biomed. Opt.* **22**(1), 010503 (2017).
29. L. Zhai, Y. Du, Y. Fu, X. Wu, "Dynamic laser speckle angiography achieved by eigen-decomposition filtering," *J. Biophotonics* **16**(9), e202300108 (2023).
30. H. S. Park, Y. C. Ahn, "Method for measuring blood flow and depth of blood vessel based on laser speckle contrast imaging using 3D convolutional neural network: A preliminary study," *Optics Laser Technol.* **179**, 111367 (2024).